

pubs.acs.org/JPCC Article

# Increasing Magnetic Hardness of Fe<sub>3</sub>Se<sub>4</sub> via Cu Doping

Luis A. Saucedo, Judith K. Clark, J. S. Raaj Vellore Winfred, Geoffrey F. Strouse, and Michael Shatruk\*



**Cite This:** *J. Phys. Chem. C* 2021, 125, 25784–25793



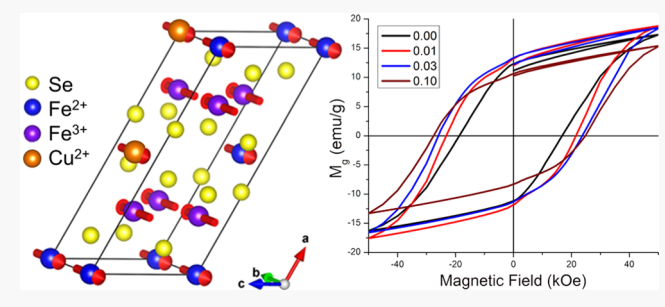
**ACCESS** I

III Metrics & More

Article Recommendations

Supporting Information

**ABSTRACT:** The influence of Cu doping on the structural and magnetic properties of the Fe<sub>3</sub>Se<sub>4</sub> ferrimagnet has been investigated by a combination of X-ray diffraction, Raman spectroscopy, X-ray absorption spectroscopy, and magnetic measurements. While the effects of dopants with ionic radii closer to those of the Fe sites in Fe<sub>3</sub>Se<sub>4</sub> had been studied before, Cu is a less conventional dopant, due to its smaller size (at the same ionic charge) and preference for lower coordination numbers. A  $(Fe_{1-x}Cu_x)_3Se_4$  series, where x = 0-0.15, has been prepared by either high-temperature annealing or the solvothermal method. Although only a limited amount of Cu enters the Fe<sub>3</sub>Se<sub>4</sub> structure, the Cu doping causes a substantial



increase in the coercivity of the material. Furthermore, the samples prepared by the solvothermal method exhibit much larger coercive fields as compared to those observed for the samples prepared by high-temperature annealing. The effect was traced to the higher lattice strain accumulated in the samples synthesized solvothermally, as evidenced by the broadening of their Raman peaks.

## ■ INTRODUCTION

The ability to control magnetic anisotropy from the atomic to mesoscale level is instrumental to the development of new magnetic materials with high-energy products. Recent years have witnessed extensive experimental<sup>2-4</sup> and theoretical<sup>5,6</sup> efforts in this direction, aimed at finding more affordable alternatives to the state-of-the-art permanent magnets that rely on the availability of costly lanthanide elements, such as neodymium, dysprosium, and samarium. Taking into account the high magnetocrystalline anisotropy offered by these elements, it is extremely challenging to eliminate them from the permanent magnets used in such critical technologies as electric motors, magnetic resonance imaging, sensors, readheads, actuators, loudspeakers, etc. Nanostructured magnetic materials, where the changes in physical properties can be controlled at a nearly atomic scale, hold promise to offer a solution to this challenge. It has been well documented that the magnetic properties of nanomaterials can vary greatly from their bulk counterparts.8 In particular, one can take advantage of the increased magnetic anisotropy observed for nanoparticles that approach the single-domain size limit. Using this approach, both theoretical  $^{9-11}$  and experimental  $^{12-16}$  models have been proposed to implement composites of nanoscale magnets to achieve magnetic hardness and energy products that exceed the values observed for any of the individual components.

Fe<sub>3</sub>Se<sub>4</sub> is a rare-earth free ferrimagnet with an ordering temperature ( $T_{\rm C}$ ) of 332 K<sup>17</sup> and a relatively high energy product of 4.37 kG Oe at 300 K.<sup>18</sup> It belongs to the Cr<sub>3</sub>S<sub>4</sub> structure type, which can be described as a variant of the NiAstype structure that lacks 50% of metal sites in every other layer

parallel to the bc plane of the monoclinic lattice (space group C2/m). These vacancy-containing layers host  $Fe^{2+}$  ions and alternate, along the a-axis, with vacancy-free layers that contain  $Fe^{3+}$  ions, with each Fe site being octahedrally coordinated by  $Se^{2-}$  ions (Figure 1a). In the magnetic structure of  $Fe_3Se_4$ , the moments on  $Fe^{2+}$  sites are aligned antiparallel to the moments on the  $Fe^{3+}$  sites, and both types of moments point along the b axis (Figure 1b). The values of the moments per Fe site, determined by neutron diffraction at 4.2 K, were 2.89  $\mu_B$  and

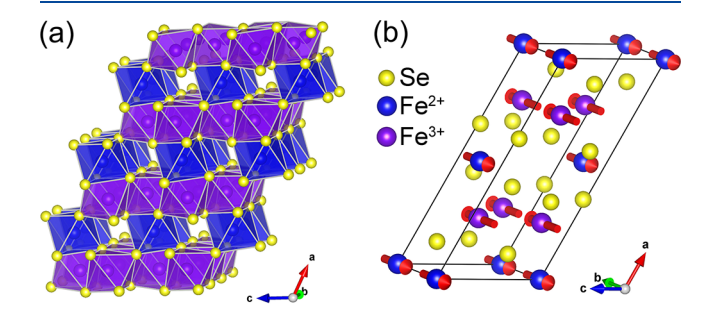


Figure 1. Crystal (a) and magnetic (b) structures of Fe $_3$ Se $_4$ , emphasizing the octahedral coordination of the Fe sites and the antiparallel moment alignment in the ferrimagnetic state.

Received: August 2, 2021 Revised: October 25, 2021 Published: November 16, 2021





2.27  $\mu_{\rm B}$ , respectively.<sup>20</sup> Given the 1:2 Fe<sup>2+</sup>/Fe<sup>3+</sup> ratio, the total saturation magnetization ( $M_{\rm s}$ ) expected at low temperatures is ~1.65  $\mu_{\rm B}$ , as was observed experimentally.

A number of studies have reported the influence of substituting other transition metals for Fe on the structural and magnetic properties of bulk Fe<sub>3</sub>Se<sub>4</sub>. The substitution by Co or Ni was found to afford solid solutions (Fe<sub>1-x</sub>M<sub>x</sub>)<sub>3</sub>Se<sub>4</sub> with the full range in the case of M = Co  $(0 \le x \le 1)$  and a limited albeit wide range for M = Ni ( $0 \le x \le 0.8$ ). In both series, the increase in the Co or Ni content led to the decrease in the  $T_{\rm C}$  and  $M_{\rm s}$  of the material.<sup>21</sup> The substitution by Ti or V proceeded to the limiting composition with x = 0.67.<sup>22</sup> The initial increase in the Ti content led to the suppression of  $T_{\rm C}$ and  $M_{\rm s}$ , but at x = 0.3 and above, a substantial change in the character of temperature-dependent magnetization curves was observed. This change was attributed to the emergence of competition between ferromagnetic (FM) and antiferromagnetic (AFM) exchange between Fe moments within the layers parallel to the bc plane. Indeed, FeTi<sub>2</sub>Se<sub>4</sub> was shown to be an antiferromagnet with the ordering temperature of 134 K.<sup>2</sup>

In contrast to the aforementioned cases, the substitution of Cr for Fe does not have such a detrimental effect on  $T_C$ . For example, Fe<sub>2</sub>CrSe<sub>4</sub> (corresponding to x = 0.33) showed  $T_C =$ 320  $\hat{K}$ , <sup>24</sup> similar to the value observed for the pristine Fe<sub>3</sub>Se<sub>4</sub>. Moreover, in the range of 0 < x < 0.33, the  $T_C$  passed through a maximum, reaching a value of 365 K at x = 0.17. The magnetic anisotropy constant  $(K_n)$  and coercivity  $(H_c)$  also increased due to the Cr substitution.<sup>25</sup> These observations were attributed to the increase in the magnetic exchange constant in  $(Fe_{1-x}Cr_x)_3Se_4$  as compared to pure  $Fe_3Se_4$ . Despite the increased coercivity, the energy product could not be greatly increased because  $M_s$  was rapidly suppressed by Cr doping. The decreased magnetic moment of the  $Cr^{3+}$  ion (S =3/2) relative to the high-spin Fe<sup>3+</sup> ion (S = 5/2) caused Fe<sub>2</sub>CrSe<sub>4</sub> to behave as a nearly compensated ferrimagnet, with the  $M_s = 0.05 \ \mu_B^{24}$ 

In an effort to increase both magnetization and coercivity, and thus achieve a higher-energy product, Sen Bishwas et al. explored the synthesis of  $(Fe_{1-x}Mn_x)_3Se_4$  nanorods. <sup>18</sup> At small doping levels (x < 0.07), the  $T_C$  and  $H_c$  values decreased only slightly, while  $M_s$  increased substantially. Due to this effect, the energy product increased by ~30% at 300 K and nearly doubled at 10 K, in comparison to the values observed for pure  $Fe_3Se_4$  nanorods. In contrast, nanosized  $(Fe_{1-x}Cr_x)_3Se_4$  showed a large increase in coercivity, which maximized at  $x \sim 0.23$ , but at the expense of a substantial decrease in magnetization, <sup>26</sup> in accord with the observations made earlier for the bulk  $(Fe_{1-x}Cr_x)_3Se_4$  samples. <sup>24</sup>

Among all of these efforts, there is no information on the effect of Cu doping on the structural and magnetic properties of Fe<sub>3</sub>Se<sub>4</sub>. A possible reason for the lack of such reports is the strong preference of Cu for tetrahedral coordination and +1 oxidation state in binary and ternary selenides. Indeed, a well-known stable structure of chalcopyrite, CuFeSe<sub>2</sub>, contains Cu<sup>+</sup> and Fe<sup>3+</sup> ions. We examined a single report on the synthesis of CuFe<sub>2</sub>Se<sub>4</sub> but found that the author, likely, had mistaken a mixture of CuFeSe<sub>2</sub> and binary iron selenides for a new ternary phase.

Given the strong preference of Cu for the tetrahedral coordination in the known Cu-containing selenides,  $^{30-34}$  we hypothesized that a minor doping of Cu into the structure of Fe<sub>3</sub>Se<sub>4</sub> might cause a substantial local structural distortion and, as a result, an increase in the coercivity of the Cu-doped Fe<sub>3</sub>Se<sub>4</sub>

due to the increased lattice strain. Herein, we report a study of the partial substitution of Cu for Fe in Fe<sub>3</sub>Se<sub>4</sub> prepared by a conventional high-temperature annealing or under solvothermal conditions typically used to decrease the particle size. We demonstrate that the bulk structure can accommodate only a very limited amount of Cu. Furthermore, we find that the synthetic method used has a substantial influence on the observed structural and magnetic properties of the Cu-doped Fe<sub>3</sub>Se<sub>4</sub>. In particular, we observe that the coercivity of Fe<sub>3</sub>Se<sub>4</sub> is greatly increased due to the lattice strain created by the solvothermal synthesis and Cu doping.

#### MATERIALS AND METHODS

Starting Materials.  $Fe_3(CO)_{12}$  (cont. 1–10% of MeOH),  $Cu(acac)_2$  ( $\geq$ 99%, acac = acetylacetonate),  $Ph_2Se_2$  (98%), octadecene (tech. 90%), and oleylamine (70%) were purchased from Sigma-Aldrich and used as received. Finely dispersed powders of iron (99.9%), copper (99.9%), and selenium (99.99%) were obtained from Alfa Aesar. The Fe and Cu powders were additionally purified by heating under a flow of  $H_2$  gas at 500 °C for 5 h and at 200 °C for 2 h, respectively.

**Synthesis**—**Method A.** The samples of  $(Fe_{1-x}Cu_x)_3Se_4$  (x = 0, 0.01, 0.02, 0.03, 0.04, 0.05) were prepared by annealing pelletized stoichiometric mixtures of elements (the total mass of each sample—300 mg) sealed in 10 mm inner diameter fused-silica tubes that were sealed under vacuum (<10<sup>-4</sup> mbar). The mixtures were heated to 1050 °C in 10.5 h, maintained at this temperature for 10 days, and quenched into an ice bath.

**Synthesis**—Method B. The samples of  $(Fe_{1-x}Cu_x)_3Se_4$  (x= 0, 0.01, 0.03, 0.05, 0.07, 0.10, 0.15) were prepared by combining Fe<sub>3</sub>(CO)<sub>12</sub> and Cu(acac)<sub>2</sub> in the required stoichiometric ratio, for a total of 0.75 mmol of the metal ions, with 234 mg (0.75 mmol) of Ph<sub>2</sub>Se<sub>2</sub> in a mixture of 8 mL of oleylamine and 2 mL of octadecene. The mixture was degassed under vacuum at 80 °C for 40 min, after which the reaction vessel was refilled with Ar and heated to 300 °C at a rate of 5 °C/min. The reaction was allowed to progress for 1 h, followed by air-cooling. The products were precipitated by sequential addition of 4 mL of hexanes and 3 mL of methanol followed by centrifugation. The isolated precipitate was washed repeatedly with hexane and methanol until the supernatant became clear and colorless. Final purification was achieved by magnetic separation using a circular Nd<sub>2</sub>Fe<sub>14</sub>B magnet to attract the product, while the supernatant solution was being filtered through a porous glass frit. The recovered product was dried by suction.

**Powder X-ray Diffraction (PXRD).** Room-temperature PXRD data were acquired on a Rigaku MiniFlex X-ray diffractometer equipped with a D/tex Ultrax detector and a Cu K $\alpha$  radiation source ( $\lambda$  = 1.54187 Å). Each pattern was recorded in the  $2\theta$  range of  $10-80^\circ$  with a step of  $0.05^\circ$  and the total collection time of 1 h. A NIST-grade LaB<sub>6</sub> powder was used as an internal standard. The analysis of PXRD patterns was carried out with SmartLab Studio II software. <sup>35</sup>

Raman Spectroscopy. Raman spectra were recorded on a Horiba JY LabRam HR Evolution spectrometer, equipped with a 600 lines/mm grating and a CCD detector. The samples were prepared as dispersed powders placed on glass slides. A 633 nm HeNe laser used for irradiation was focused on the sample with an x50 LWD objective lens. The spectra were collected in the range of 100–700 cm<sup>-1</sup>.

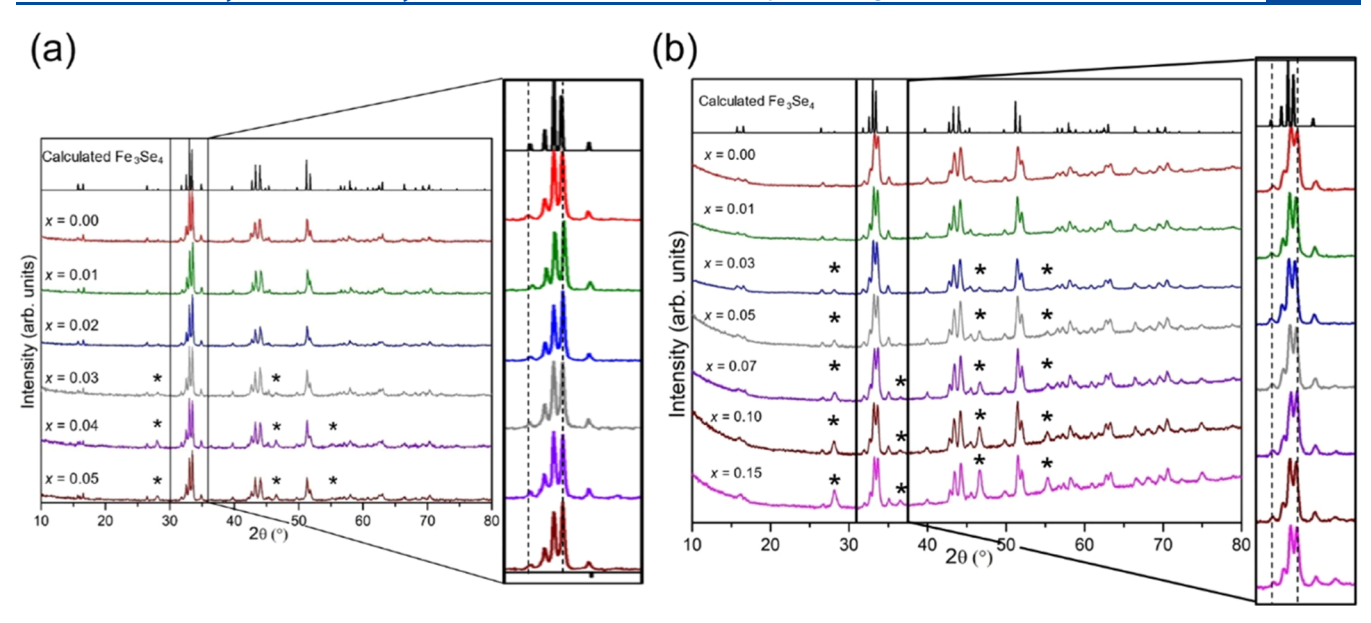


Figure 2. PXRD patterns for the  $(Fe_{1-x}Cu_x)_3Se_4$  samples prepared by Methods A (a) and B (b). The asterisks indicate the peaks of the CuFeSe<sub>2</sub> byproduct. The insets show enlarged regions of the patterns revealing the shift in the peak positions caused by the doping of Cu into the structure of Fe<sub>3</sub>Se<sub>4</sub>.

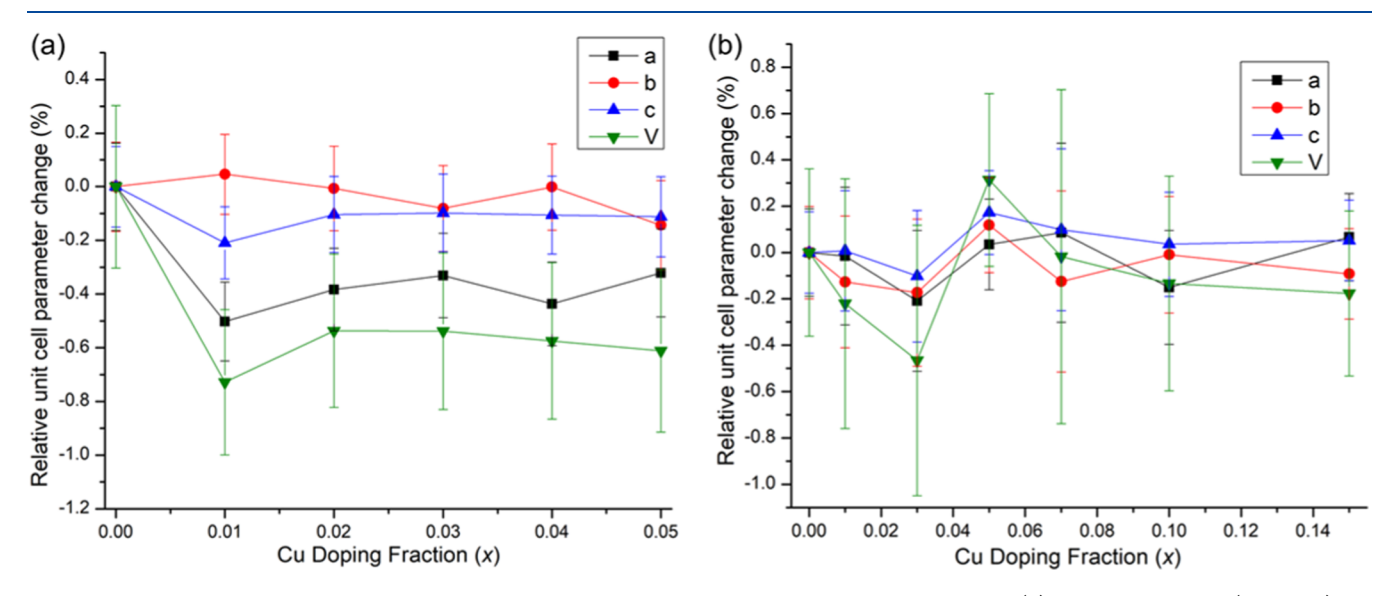


Figure 3. Relative changes in unit cell parameters and volume as a function of the Cu doping fraction (x) in the samples of  $(Fe_{1-x}Cu_x)_3Se_4$  prepared by Methods A (a) and B (b). The lines connecting the data points are guides for the eye.

**X-ray Absorption Near-Edge Structure (XANES) Spectroscopy.** XANES spectra were collected at beamline 9-BM of the Advanced Photon Source (APS) at Argonne National Laboratory. Powder samples of  $(Fe_{1-x}Cu_x)_3Se_4$ , containing 15% by mass of polyethylene glycol, were pelletized, mounted on a carbon tape, and covered with a Mylar film. The measurements were performed in a fluorescence mode using a PIPIS detector. The scans were taken at Fe and Cu K-edges for each sample. Calibrations were done on films of Fe or Cu for the corresponding K-edges. The data were processed and analyzed with the Athena subroutine of the IFEFFIT software. For each sample, 3 Fe and 12 Cu K-edge spectra were combined and averaged to improve the data quality.

**Magnetic Measurements.** Magnetic properties were studied with a magnetic property measurements system, MPMS-XL (Quantum Design), equipped with a superconducting quantum interference device (SQUID). Samples

were weighed and packed in polycarbonate capsules and covered with 1-eicosane wax to prevent the reorientation of particles during magnetic measurements. Temperature-dependent zero-field-cooled (ZFC) and field-cooled (FC) magnetization data were measured in a constant applied magnetic field of 100 Oe at a sweep rate of 2 K/min. Field-dependent isothermal hysteresis loops were measured at 5 and 250 K with the applied field varying from -50 to 50 kOe.

### ■ RESULTS AND DISCUSSION

**Synthesis.** Method A for the synthesis of  $(Fe_{1-x}Cu_x)_3Se_4$  followed the conventional annealing protocol. The pelletized stoichiometric mixtures of elements were annealed at 1050 °C for  $\sim$ 10 days, followed by quenching the reactions into an ice bath. In a typical synthesis of bulk or doped  $Fe_3Se_4$  reported previously, the annealing was performed at 800–900 °C, after

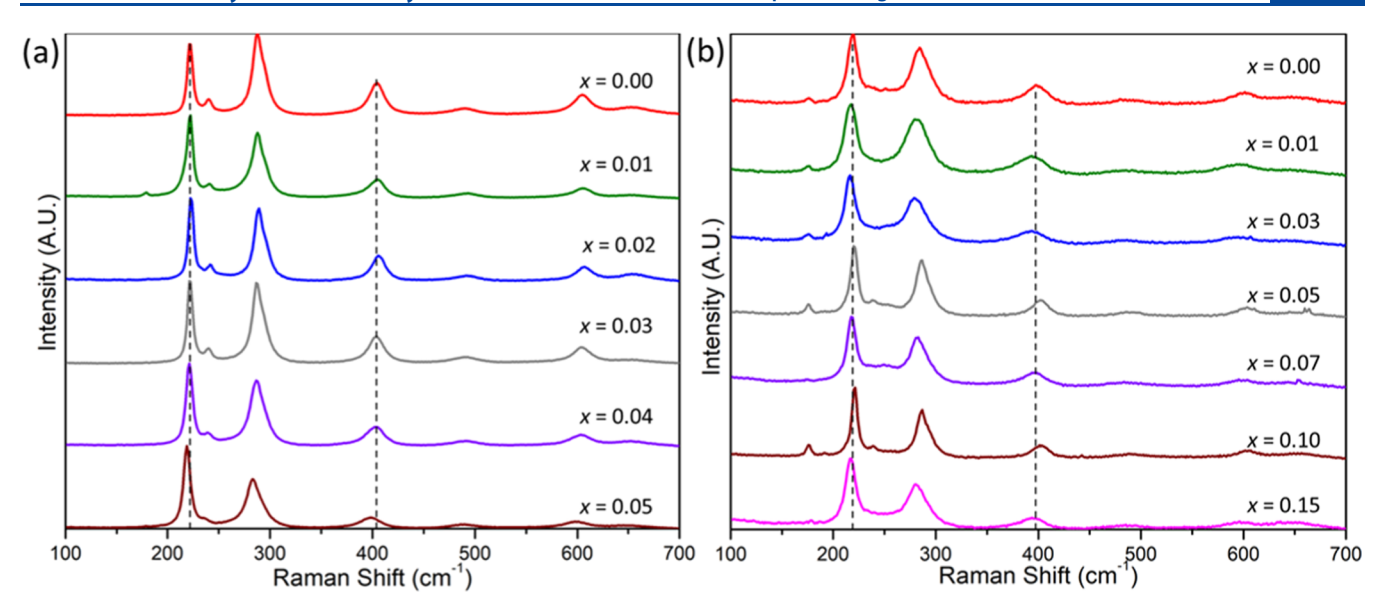


Figure 4. Raman spectra of the  $(Fe_{1-x}Cu_x)_3Se_4$  samples prepared by Methods A (a) and B (b). The dashed vertical lines, which cross the energy axis at 220 and 400 cm<sup>-1</sup>, are guides for the eye.

which the samples were reground and reannealed at the same or slightly lower temperature to obtain single-phase products. We found that such an annealing regime, in the presence of Cu, led to the formation of the stable CuFeSe<sub>2</sub> phase as a major byproduct. By increasing the reaction temperature to 1050 °C and quenching the samples, we were able to obtain phase-pure products without the need for the additional annealing step.

In Method B, the  $(Fe_{1-x}Cu_x)_3Se_4$  samples were prepared by reacting Ph<sub>2</sub>Se<sub>2</sub>, Fe<sub>3</sub>(CO)<sub>12</sub>, and Cu(acac)<sub>2</sub> in a mixed oleylamine/octadecene solvent (4:1 v/v), with the goal to reduce the particle size to nanoscale. As will be shown below, such a route succeeded in producing smaller particles but only at the submicron scale (Figure S1). Previously reported solvothermal syntheses of Fe<sub>3</sub>Se<sub>4</sub> employed Fe(acac)<sub>3</sub> and elemental Se powder in oleylamine, 38-40 or even a solvothermal reaction between the powders of Fe and Se.<sup>41</sup> These precursors, however, are prone to the formation of oxides at elevated temperatures, and an excess of Se might be difficult to remove from the reaction products. We found that the use of Fe<sub>3</sub>(CO)<sub>12</sub> and Ph<sub>2</sub>Se<sub>2</sub> circumvented such problems, and pristine or Cu-doped Fe<sub>3</sub>Se<sub>4</sub> samples were obtained by reactions carried out in oleylamine/octadecene at 300 °C for 1 h. It is also important to note that, in comparison to the traditional synthetic routes that used Fe(acac)<sub>3</sub> and Se as starting materials, we did not observe a ferrimagnetic Fe<sub>7</sub>Se<sub>8</sub> impurity in any of our samples.

For brevity, from this point forward, we will refer to the samples prepared by high-temperature annealing and solvo-thermal methods as A-samples and B-samples, respectively.

**Crystal Structure.** PXRD analysis (Figure 2) of the Asamples of  $(Fe_{1-x}Cu_x)_3Se_4$  revealed that single-phase products are obtained at lower Cu content, up to x = 0.02. For samples with  $x \ge 0.03$ , peaks corresponding to the CuFeSe<sub>2</sub> byproduct became visible, growing in intensity as the value of x increased. Thus, it appears that the maximum amount of Cu that can be cleanly doped for Fe in the structure of Fe<sub>3</sub>Se<sub>4</sub> is 2% if the conventional high-temperature annealing is used. Unit cell constants were determined by the LeBail fitting procedure (Figure S2). The parameters a and c and the cell volume

showed a relatively large initial decrease for x = 0.01 before a slight recovery at x = 0.02, after which they remained nearly constant (Figure 3a). The decrease in the unit cell volume is primarily due to the large decrease in the a parameter, which corresponds to the direction of the stacking of alternating layers of Fe<sup>2+</sup> and Fe<sup>3+</sup> ions, as shown in Figure 1. The exact values of unit cell parameters and volume refined from the PXRD patterns are listed in Table S1.

One should not discard the scenario where Cu might be entering vacant octahedral sites to form a filled structure of  $Fe_3Se_4$ , given the possibility to vary the  $Fe^{2+}/Fe^{3+}$  ratio to compensate for the positive charge brought by such Cu intercalation. We attempted to prepare samples with excess Cu, corresponding to the composition  $(FeCu_x)_3Se_4$ , but such attempts led to the formation of  $CuFeSe_2$  and  $Fe_7Se_8$  (Figure S3), thus suggesting that it is very unlikely that Cu atoms populate the vacant octahedral sites in the  $Fe_3Se_4$  structure.

In contrast to the annealed A-samples, the B-samples of  $(Fe_{1-x}Cu_x)_3Se_4$ , obtained by the solvothermal method, showed negligible changes in unit cell parameters and volume as a function of x, within the experimental error (Figure 3b). Similar to the A-samples, the B-samples contained the minor  $CuFeSe_2$  byproduct already seen at x=0.03, and the amount of this byproduct increased with x (Figure 2b).

Raman Spectroscopy. To gain insight into the effect of substitution on the lattice strain of the material, the pure and Cu-doped samples of Fe<sub>3</sub>Se<sub>4</sub> were examined by Raman spectroscopy. The undoped Fe<sub>3</sub>Se<sub>4</sub> showed Raman peaks with maxima at 221, 240, 288, 405, 489, and 605 cm<sup>-1</sup> for the A-sample (Figure 4a) and at 219, 284, 397, 484, and 601 cm<sup>-1</sup> for the B-sample (Figure 4b). The only previous study of Raman spectra for Fe<sub>3</sub>Se<sub>4</sub> reported similar peaks in the given energy range and briefly attributed the peaks at 228 and 411 cm<sup>-1</sup> to lattice vibrations. 18 Using Porto's nuclear site group analysis, 42 we find that possible Raman-active vibrations for Fe<sub>3</sub>Se<sub>4</sub> include 6A<sub>g</sub> and 3B<sub>g</sub> modes. The strong Raman modes observed at 221/219 and 288/284 cm<sup>-1</sup> correspond to the energy of Fe-Se bond vibrations, and the observation of two such modes is in agreement with the anisotropy (low symmetry) of the crystal structure. The peaks at 405/397

and  $605/601 \text{ cm}^{-1}$  are likely overtone frequencies of the 221/219 cm<sup>-1</sup> vibration, showing increased anharmonicity when moving to higher overtones (as judged by the increased asymmetry of the peaks). On the other hand, the peak at 489/484 cm<sup>-1</sup> is likely a combination mode of Fe–Se vibrations observed at 221/219 and 288/284 cm<sup>-1</sup>. Interestingly, all B-samples and the A-sample with x = 0.01 showed a weak Raman peak at  $\sim 180 \text{ cm}^{-1}$ . The nature of this peak is yet unclear.

With the substitution of Cu for Fe, the Raman peaks in the A-samples show a tendency to shift to lower energies at the higher Cu content (Figure 5 and Table S2). This shift also

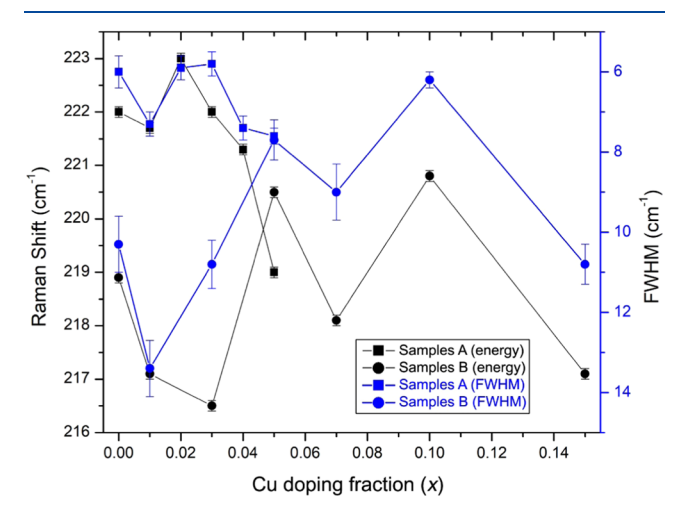


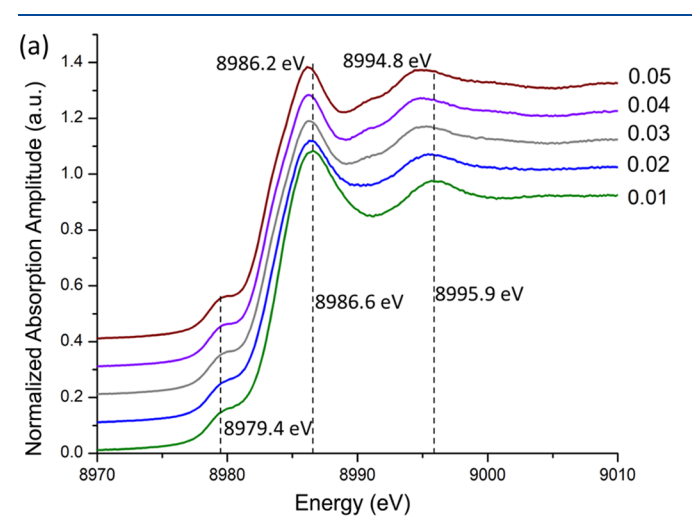
**Figure 5.** Variation of the energy (black) and FWHM (blue) for the  $221/219 \, \mathrm{cm}^{-1}$  Raman peak as a function of the Cu content (x) for the  $(\mathrm{Fe}_{1-x}\mathrm{Cu}_x)_3\mathrm{Se}_4$  samples prepared by Methods A (square boxes) and B (circles), respectively.

correlates with the peak broadening, as evidenced by the larger full width at half-maximum (FWHM) of the Raman peaks observed for the samples with the larger values of x. The broadening becomes especially obvious for the peaks at 240 and 400 cm $^{-1}$ , the amplitude of which is substantially diminished (Figure 4a). Interestingly, the FWHM correlates with the shift in the peak maximum (Figure 5). Thus, doping

Cu into the  $Fe_3Se_4$  lattice leads to the increased lattice strain, as could be expected from the difference in the radii of the corresponding ions (Table S3) and the preference of Cu for lower coordination numbers.<sup>43</sup>

The B-samples showed much less consistency in the energy and FWHM of the Raman peaks. The values of these parameters vary widely from sample to sample, and the peak widths, in general, are substantially larger than those observed for the A-samples. We attribute this inconsistency to the higher strain accumulated in the B-samples during the solvothermal synthesis. It is quite reasonable to assume that the high-temperature annealing, undergone by the A-samples, relieved the strain in the lattice. Indeed, the larger FWHM observed for the B-samples is comparable to the FWHM of the Raman peaks reported for the Mn-doped samples of Fe<sub>3</sub>Se<sub>4</sub>, which were also prepared by a solvothermal method.<sup>18</sup>

XANES Spectroscopy. To establish the nature of Cu dopants in all samples, room-temperature XANES spectra were collected at the Cu and Fe K-edges. As mentioned in the Introduction section, one of the motivations for our work was the knowledge that the oxidation state of +1 had been typically observed for Cu in various selenides. Nevertheless, the Cu Kedge spectra of both A-samples and B-samples exhibit a weak pre-edge feature at 8979.5 eV (Figure 6), which can be assigned only to the dipole-forbidden 1s  $\rightarrow$  3d transition of the Cu<sup>2+</sup> ion with the single hole in the 3d orbitals.<sup>44</sup> This assignment is also supported by the fact that the XANES spectrum of Cu<sub>2</sub>Se does not show such a pre-edge feature, with the absorption edge appearing at a notably higher energy, 8982 eV. 45 In typical Cu K-edge spectra of Cu(I) compounds, the absorption edge characteristic of the Cu<sup>+</sup> ion appears in the 8983-8985 eV range. 46 In contrast, both samples A (Figure 6a) and samples B (Figure 6b) show the absorption edge at ~8986 eV, which is also characteristic of the Cu<sup>2+</sup> ion. A small contribution from the absorption in the range typical of Cu<sup>+</sup> ions might be present for the B-samples, as judged by the asymmetry of the strong absorption peak (Figure 6b). Our analysis is also supported by the reported XANES spectra of CuO and Cu2O. While the absorption edge was observed at lower energy for Cu<sub>2</sub>O, the spectrum of CuO showed a weak



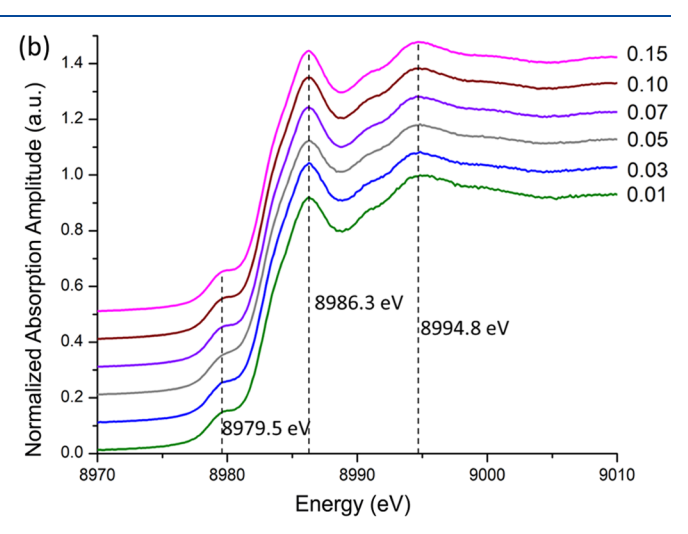


Figure 6. Normalized Cu K-edge XANES spectra for the  $(Fe_{1-x}Cu_x)_3Se_4$  samples prepared by Methods A (a) and B (b). The vertical dashed lines are guides for the eye at the given energy values. The spectra of different samples have been shifted along the vertical axis for the ease of comparison.

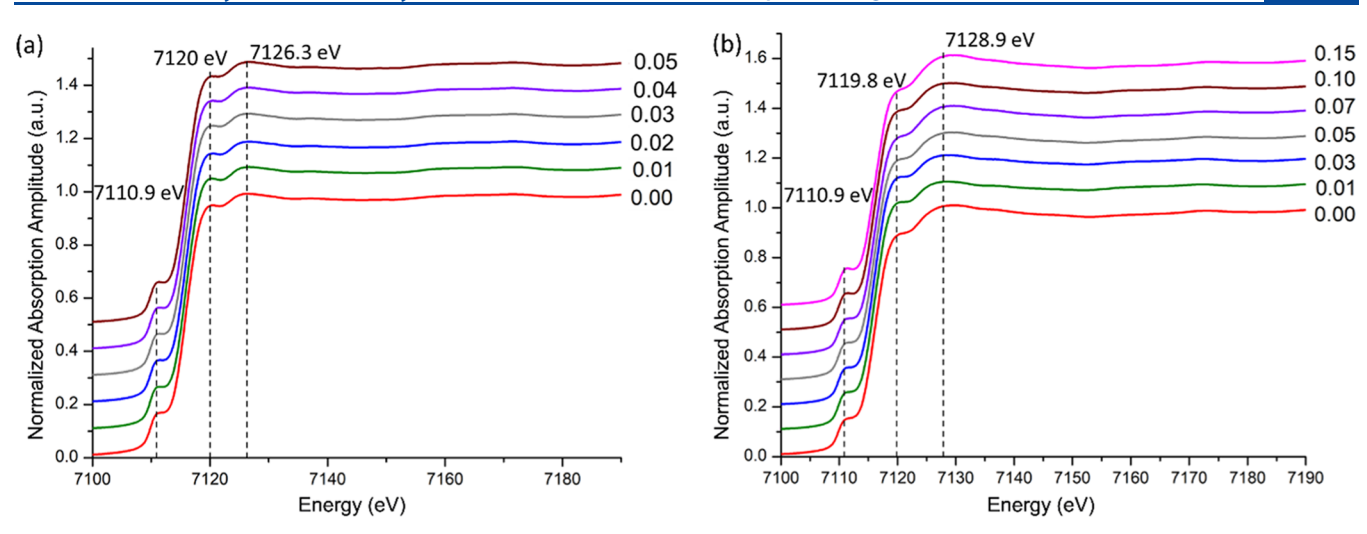


Figure 7. Normalized Fe K-edge XANES spectra for the  $(Fe_{1-x}Cu_x)_3Se_4$  samples prepared by Methods A (a) and B (b). The vertical dashed lines are guides for the eye at the given energy values. The spectra of different samples have been shifted along the vertical axis for the ease of comparison.

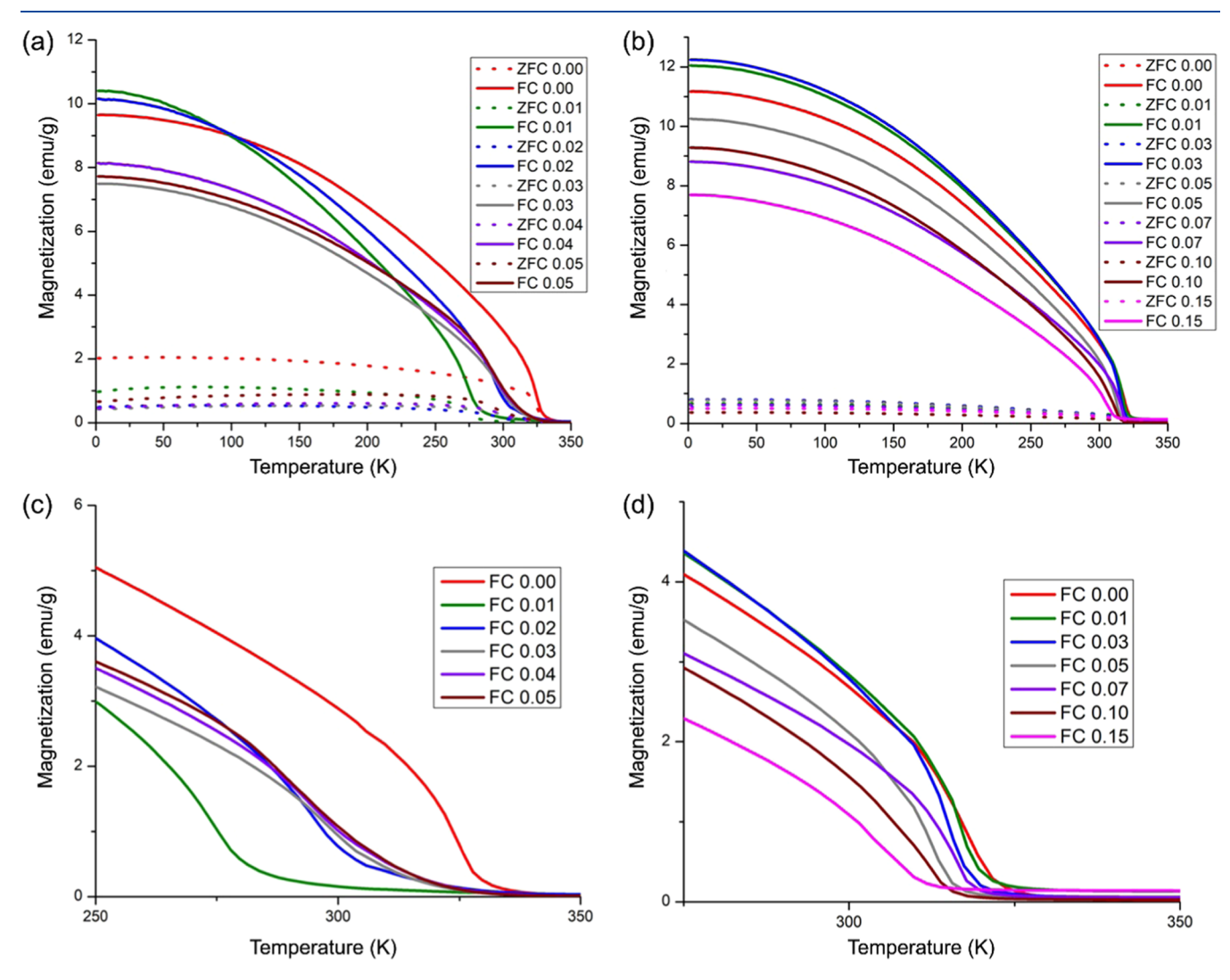


Figure 8. Temperature dependence of the ZFC and FC magnetization recorded under an applied magnetic field of 100 Oe for the  $(Fe_{1-x}Cu_x)_3Se_4$  samples prepared by Methods A (a) and B (b). Panels (c) and (d) show enlarged parts of the corresponding ZFC-FC plots around the ordering temperature. The nominal Cu doping fraction (x) is given in the legends.

Table 1. Magnetic Properties of the (Fe<sub>1-x</sub>Cu<sub>x</sub>)<sub>3</sub>Se<sub>4</sub> Samples Prepared by Methods A and B

A-samples	$T_{\rm C}$ (K)	$H_{\rm c}$ (kOe)	$M_{\rm r}$ (emu/g)	B-samples	$T_{\rm C}$ (K)	$H_{c}$ (kOe)	$M_{\rm r}$ (emu/g)
x = 0.00	330	3.0	9.1	x = 0.00	323	17.7	12.3
x = 0.01	286	5.8	11.1	x = 0.01	322	22.4	13.2
x = 0.02	305	4.7	12.3	x = 0.03	321	24.8	13.3
x = 0.03	310	2.3	10.1	x = 0.05	317	25.0	9.7
x = 0.04	315	1.9	8.7	x = 0.07	319	24.9	9.2
x = 0.05	315	0.7	4.8	x = 0.10	316	26.2	10.6
				x = 0.15	311	25.2	8.1

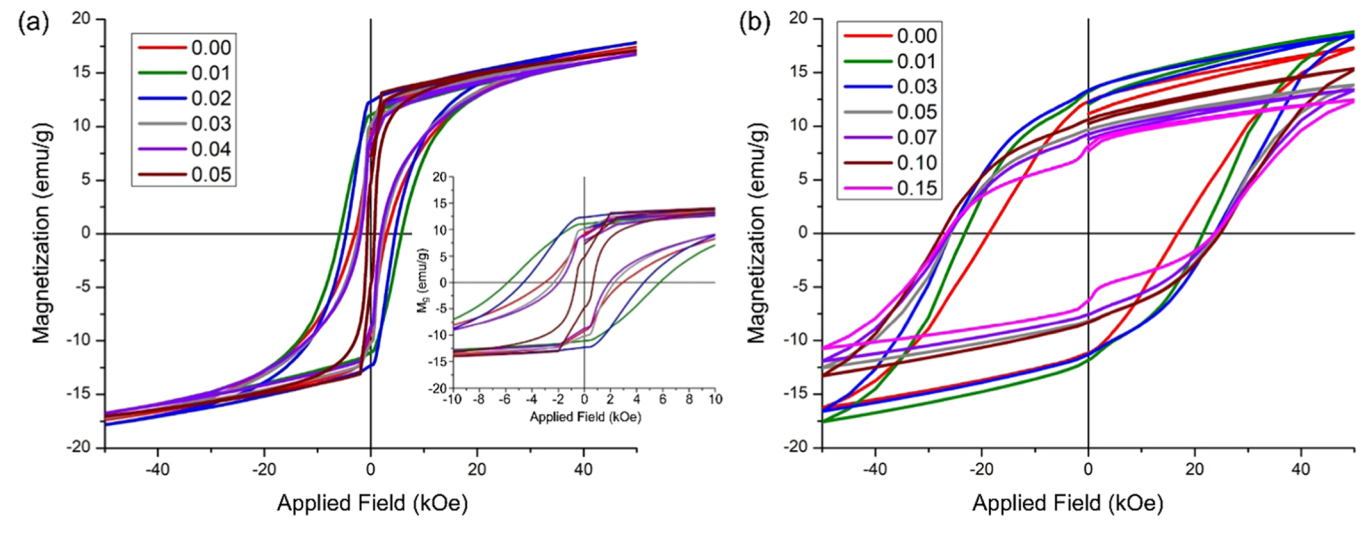


Figure 9. Field-dependent magnetization recorded at 5 K for the  $(Fe_{1-x}Cu_x)_3Se_4$  samples prepared by Methods A (a) and B (b). The inset shows the enlarged hysteresis region for the A-samples at lower fields. The nominal Cu doping fraction (x) is given in the legends.

pre-edge feature located at a slightly lower energy than that of the absorption edge of  $\text{Cu}_2\text{O.}^{47}$ 

Examination of the Fe K-edge XANES spectra reveals three absorption features common for all the samples (Figure 7). Similar spectra were obtained in the only other reported XANES study of Fe<sub>3</sub>Se<sub>4</sub>. The energies of the absorption peaks and the overall nature of the Fe K-edge spectra remain almost unchanged upon Cu doping, suggesting that the local structure around the Fe sites is essentially preserved. The preedge feature at 7110.9 eV corresponds to the dipole-forbidden  $1s \rightarrow 3d$  transition. The two higher-energy absorption features correspond to 1s  $\rightarrow$  4p transitions, with the first of them observed as a shoulder at  $\sim$ 7120 eV for both series of samples. The third, highest in energy absorption feature, shows the largest difference between the two series of samples, as this peak appears at 7126.3 eV for the A-samples and at 7128.9 eV for the B-samples. This energy difference may suggest the presence of a higher amount of Fe<sup>3+</sup> sites in the B-samples, as such shifts of spectral features to the higher energy have been attributed to the higher oxidation state of Fe. 49 Such an effect can be caused by a slight cation deficiency of the B-samples prepared by the solvothermal method.

**Magnetic Properties.** The temperature-dependent magnetization measured under an applied field of 100 Oe revealed the divergence between the ZFC and FC magnetization curves, characteristic of ferrimagnetic ordering (Figure 8). The Curie temperature ( $T_{\rm C}$ ), determined as the ZFC-FC divergence point, was equal to 330 K for the undoped A-sample and 323 K for the undoped B-sample. The summary of the ordering temperatures and other magnetic parameters for all samples is given in Table 1. With the increase in the Cu content, the value

of  $T_{\rm C}$  is gradually suppressed across the B-series, reaching the lowest value of 311 K at x = 0.15. In contrast, the value of  $T_C$ in the A-series initially experiences a substantial drop to 286 K for x = 0.01 but then recovers and slightly increases (from 305) to 315 K) for the samples with the higher Cu content. Interestingly, such behavior correlates with the larger FWHM of the  $\sim$ 220 cm<sup>-1</sup> Raman peak observed for the A-sample with x = 0.01 as compared to the FWHM of this peak for the Asamples with x = 0, 0.02, and 0.03 (Figure 4), suggesting that the lattice strain increases with the initial Cu doping but then slightly relaxes. We would like to point out that the presence of the minor CuFe<sub>2</sub>Se<sub>2</sub> impurity does not affect the magnetism of samples A and B. The AFM transition that takes place in  $\text{CuFeSe}_2$  at 70  $\text{K}^{50}$  is not observed in the measured ZFC and FC magnetization curves, thus indicating a negligible contribution from this impurity to the overall response from the main ferrimagnetic phase.

The increase in the lattice strain typically leads to the higher magnetic anisotropy of the material. In accord with this expectation, 5 K isothermal magnetization measurements on the A-samples (Figure 9a) revealed a large increase in the coercive field ( $H_c$ ) when going from x=0 (3.8 kOe) to 0.01 (5.8 kOe). With further increase in the Cu doping fraction, the  $H_c$  value gradually decreases, falling to 0.7 kOe at x=0.05 (Table 1). The remnant magnetization ( $M_r$ ) increases from 9.1 emu/g for x=0 to 12.3 emu/g for x=0.02, after which it gradually decreases, reaching the value of 4.8 emu/g at x=0.05.

Remarkably, all B-samples showed a much higher coercivity as compared to the A-samples, in agreement with the substantially higher lattice strain deduced from the broader

Raman peaks observed for the B-series. The coercivity increases abruptly, from 17.7 kOe for the B-sample with x=0 to 22.4 kOe for the one with x=0.01, and then more gradually, reaching a maximum value of 26.2 kOe at x=0.10. The samples prepared by the solvothermal method also exhibit a notable exchange bias effect, observed as asymmetry in the hysteresis loops (Figure 9b). The exchange bias might indicate minor surface oxidation that leads to the presence of a thin layer of antiferromagnetic phase that couples to the underlying ferrimagnetic phase. Similar to the A-samples, the remnant magnetization of the B-samples increases with the initial Cu doping but then decreases at higher values of x, although not as quickly as observed for the A-series.

### CONCLUDING REMARKS

As demonstrated by the combined results of PXRD, Raman and XANES spectroscopy, and magnetic measurements, the properties of  $(Fe_{1-x}Cu_x)_3Se_4$  samples show substantial differences, depending on the synthetic method. The main source of these differences is the lattice strain, which appears to be much higher in the samples prepared solvothermally (Method B) as compared to the samples prepared by high-temperature annealing (Method A). While the presence of this effect was hypothesized based on the broader Raman peaks observed for the B-samples, its most dramatic manifestation is the much larger magnetic coercivity (anisotropy) of the B-samples as compared to the A-samples (Figure 9).

Interestingly, however, the lattice parameters of the B-samples show less obvious changes upon Cu doping as compared to those of the A-samples, although the Cu K-edge XANES spectra are similar for both series of the  $(Fe_{1-x}Cu_x)_3Se_4$  samples. It is likely that the true level of Cu doping in the B-samples is substantially lower than the nominal value of x, as also evidenced by the increase in the quantity of the CuFeSe<sub>2</sub> byproduct for the B-samples with x > 0.03.

Despite the low level of Cu dopant sites that can be introduced into the Fe<sub>3</sub>Se<sub>4</sub> structure, the presence of such dopants has a strong impact on the magnetic anisotropy of the material. For both methods of the sample preparation, the magnetic coercivity abruptly increases for the Cu doping fraction as small as x = 0.01. We attribute this initial increase in magnetic anisotropy to the lattice strain caused by the smaller size of the Cu<sup>2+</sup> ions relative to the average size of the Fe<sup>2+</sup> and Fe<sup>3+</sup> ions and the preference of Cu for lower coordination numbers.

Overall, this work demonstrates that the use of unconventional dopants offers a viable strategy for increasing the magnetic hardness of  $\mathrm{Fe_3Se_4}$ . In fact, such doping induces a substantial lattice strain, due to the large difference in the ionic radii and coordination preferences of the Fe sites and the dopant ion. At the same time, the low level of doping does allow preservation of the high magnetic ordering temperature and even a slight increase in the remnant magnetization, thus increasing the overall energy product. Our future efforts will focus on a more thorough investigation of the nature of local structural distortions around the dopant ions and the changes in magnetostriction caused by the increased lattice strain. The results of these studies will be reported in due course.

## ASSOCIATED CONTENT

#### Supporting Information

The Supporting Information is available free of charge at https://pubs.acs.org/doi/10.1021/acs.jpcc.1c06841.

SEM images with energy dispersive X-ray analysis (EDX) analysis results, PXRD patterns with LeBail profile fitting, a listing of unit cell parameters and Raman peaks, and a tabulation of relevant ionic radii (PDF)

#### AUTHOR INFORMATION

#### **Corresponding Author**

Michael Shatruk — Department of Chemistry and Biochemistry, Florida State University, Tallahassee, Florida 32306, United States; orcid.org/0000-0002-2883-4694; Email: shatruk@chem.fsu.edu

#### **Authors**

- Luis A. Saucedo Department of Chemistry and Biochemistry, Florida State University, Tallahassee, Florida 32306, United States
- Judith K. Clark Department of Chemistry and Biochemistry, Florida State University, Tallahassee, Florida 32306, United States
- J. S. Raaj Vellore Winfred Department of Chemistry and Biochemistry, Florida State University, Tallahassee, Florida 32306, United States
- Geoffrey F. Strouse Department of Chemistry and Biochemistry, Florida State University, Tallahassee, Florida 32306, United States; ⊚ orcid.org/0000-0003-0841-282X

Complete contact information is available at: https://pubs.acs.org/10.1021/acs.jpcc.1c06841

#### Notes

The authors declare no competing financial interest.

### ACKNOWLEDGMENTS

This work was supported by the U.S. National Science Foundation (award DMR-1905499 to M.S.). L.A.S. thanks the Florida Education Fund for the McKnight Doctoral Fellowship. This project used resources provided by the X-ray Crystallography Center (FSU075000XRAY) and the Materials Characterization Laboratory (FSU075000MAC) at the Department of Chemistry and Biochemistry, Florida State University.

#### REFERENCES

- (1) Gutfleisch, O.; Willard, M. A.; Brück, E.; Chen, C. H.; Sankar, S. G.; Liu, J. P. Magnetic materials and devices for the 21<sup>st</sup> century: stronger, lighter, and more energy efficient. *Adv. Mater.* **2011**, 23, 821–842.
- (2) Shao, Z.; Ren, S. Rare-earth-free magnetically hard ferrous materials. *Nanoscale Adv.* **2020**, *2*, 4341–4349.
- (3) Cui, J.; Kramer, M.; Zhou, L.; Liu, F.; Gabay, A.; Hadjipanayis, G.; Balasubramanian, B.; Sellmyer, D. Current progress and future challenges in rare-earth-free permanent magnets. *Acta Mater.* **2018**, 158, 118–137.
- (4) Patel, K.; Zhang, J.; Ren, S. Rare-earth-free high energy product manganese-based magnetic materials. *Nanoscale* **2018**, *10*, 11701–11718.
- (5) Vishina, A.; Vekilova, O. Y.; Björkman, T.; Bergman, A.; Herper, H. C.; Eriksson, O. High-throughput and data-mining approach to predict new rare-earth free permanent magnets. *Phys. Rev. B* **2020**, *101*, No. 094407.
- (6) Gao, Q.; Opahle, I.; Gutfleisch, O.; Zhang, H. Designing rarearth free permanent magnets in Heusler alloys via interstitial doping. *Acta Mater.* **2020**, *186*, 355–362.
- (7) Coey, J. M. D. Permanent magnet applications. *J. Magn. Magn. Mater.* **2002**, 248, 441–456.

- (8) Guimarães, A. P. *Principles of Nanomagnetism*; Springer-Verlag: Berlin-Heidelberg, 2009.
- (9) Skomski, R.; Coey, J. M. D. Giant energy product in nanostructured two-phase magnets. *Phys. Rev. B* **1993**, 48, 15812–15816
- (10) Goto, E.; Hayashi, N.; Miyashita, T.; Nakagawa, K. Magnetization and switching characteristics of composite thin magnetic films. *J. Appl. Phys.* **1965**, *36*, 2951–2958.
- (11) Kneller, E. F.; Hawig, R. The exchange-spring magnet: a new material principle for permanent magnets. *IEEE Trans. Magn.* **1991**, 27, 3588–3600.
- (12) Zeng, H.; Li, J.; Liu, J. P.; Wang, Z. L.; Sun, S. H. Exchange-coupled nanocomposite magnets by nanoparticle self-assembly. *Nature* **2002**, *420*, 395–398.
- (13) Liu, F.; Zhu, J. H.; Yang, W. L.; Dong, Y. H.; Hou, Y. L.; Zhang, C. Z.; Yin, H.; Sun, S. H. Building nanocomposite magnets by coating a hard magnetic core with a soft magnetic shell. *Angew. Chem., Int. Ed.* **2014**, 53, 2176–2180.
- (14) Yang, W.; Lei, W.; Yu, Y.; Zhu, W.; George, T. A.; Li, X. Z.; Sellmyer, D. J.; Sun, S. From FePt–Fe<sub>3</sub>O<sub>4</sub> to L1<sub>0</sub>-FePt–Fe nanocomposite magnets with a gradient interface. *J. Mater. Chem. C* **2015**, *3*, 7075–7080.
- (15) Carnevale, D. J.; Shatruk, M.; Strouse, G. F. Ligand passivated core-shell FePt@Co nanomagnets exhibiting enhanced energy product. *Chem. Mater.* **2016**, 28, 5480–5487.
- (16) Li, D.; Wang, H.; Ma, Z.; Liu, X.; Dong, Y.; Liu, Z.; Zhang, T.; Jiang, C. FePt/Co core/shell nanoparticle-based anisotropic nanocomposites and their exchange spring behavior. *Nanoscale* **2018**, *10*, 4061–4067.
- (17) Ozawa, K.; Yoshimi, T.; Anzai, S.; Yanagisawa, S. Effect of pressure on the ferrimagnetic Curie temperature of Fe<sub>3</sub>□Se<sub>4</sub>. *Phys. Status Solidi A* **1973**, *19*, K39−K41.
- (18) Sen Bishwas, M.; Das, R.; Poddar, P. Large increase in the energy product of Fe<sub>3</sub>Se<sub>4</sub> by Fe-site doping. *J. Phys. Chem. C* **2014**, 118, 4016–4022.
- (19) Hayashi, A.; Imada, K.; Inoue, K.; Ueda, Y.; Kosuge, K. Phase diagram of metal selenides  $(M_x'M_{1-x})_3Se_4$  ( $0 \le x \le 1$ ) (M, M' = 3d-transition metals). Bull. Inst. Chem. Res., Kyoto Univ. 1986, 64, 186–206.
- (20) Andresen, A. F.; Van Laar, B. Magnetic structure of Fe<sub>3</sub>Se<sub>4</sub>. *Acta Chem. Scand.* **1970**, 24, 2435–2439.
- (21) Kojima, K.; Murase, S.; Sato, K.; Adachi, K. Magnetic properties of  $(Fe_{1-x}M_x)_3Se_4$ : M=Ni and Co. J. Phys. Soc. Jpn. 1970, 29, 1642.
- (22) Hayashi, A.; Kishi, T.; Ueda, Y.; Kosuge, K. Phase diagram and magnetic properties of the  $(Fe_xTi_{1-x})_3Se_4$  system. *Mater. Res. Bull.* 1989, 24, 701–710.
- (23) Hirakawa, K. The magnetic properties of iron selenide single crystals. *J. Phys. Soc. Jpn.* **1957**, *12*, 929–938.
- (24) Regnard, J. R.; Chappert, J. 3d-electron delocalization in the semi-metallic compounds  $MFe_2Se_4$  with M=Ti, Cr, Fe, Co, Ni. *J. Phys.* **1973**, 34, 721–731.
- (25) Li, D.; Li, S. J.; Dong, B. J.; Yang, T.; Liu, W.; Zhang, Z. D. Large magnetocrystalline anisotropy of Fe<sub>3-x</sub>Cr<sub>x</sub>Se<sub>4</sub> single crystals due to Cr substitution. *Europhys. Lett.* **2015**, *109*, No. 37004.
- (26) Li, S.-j.; Li, D.; Liu, W.; Zhang, Z. High Curie temperature and coercivity performance of Fe<sub>3-x</sub>Cr<sub>x</sub>Se<sub>4</sub> nanostructures. *Nanoscale* **2015**, *7*, 5395–5402.
- (27) Delgado, J. M.; de Delgado, G. D.; Quintero, M.; Woolley, J. C. The crystal structure of copper iron selenide, CuFeSe<sub>2</sub>. *Mater. Res. Bull.* **1992**, 27, 367–373.
- (28) Reddy, K. V.; Chetty, S. C. Mössbauer studies on CuFeSe<sub>2</sub>. Mater. Res. Bull. 1976, 11, 55-60.
- (29) Lee, C. S. X-ray and Mössbauer studies of CuFe<sub>2</sub>Se<sub>4</sub>. Bull. Natl. Fish. Univ. Busan 1982, 22, 37–40.
- (30) Yamamoto, K.; Kashida, S. X-ray study of the average structures of Cu<sub>2</sub>Se and Cu<sub>1.8</sub>S in the room temperature and the high temperature phases. *J. Solid State Chem.* **1991**, *93*, 202–211.

- (31) Bongers, P. F.; Van Bruggen, C. F.; Koopstra, J.; Omloo, W. P. F. A. M.; Wiegers, G. A.; Jellinek, F. Structures and magnetic properties of some metal (I) chromium (III) sulfides and selenides. *J. Phys. Chem. Solids* **1968**, *29*, 977–984.
- (32) Daszkiewicz, M.; Gulay, L. D.; Shemet, V. Y.; Pietraszko, A. Comparative investigation of the crystal structure of  $LnCuSe_2$  compounds (Ln = Tb, Dy, Ho, Er, Tm, Yb and Lu). Z. Anorg. Allg. Chem. 2008, 634, 1201–1204.
- (33) Klepp, K. O.; Gurtner, D. Crystal structure of tricopper tetraselenidovanadate(V),  $Cu_3VSe_4$ . Z. Kristallogr. New Cryst. Struct. **2000**, 215, No. 4.
- (34) Fan, J.; Carrillo-Cabrera, W.; Akselrud, L.; Antonyshyn, I.; Chen, L.; Grin, Y. New monoclinic phase at the composition Cu<sub>2</sub>SnSe<sub>3</sub> and its thermoelectric properties. *Inorg. Chem.* **2013**, *52*, 11067–11074.
- (35) Rigaku Corporation. Integrated X-ray diffraction software SmartLab Studio II. Rigaku J. 2015, 31, 25–26.
- (36) Ravel, B.; Newville, M. ATHENA, ARTEMIS, HEPHAESTUS: data analysis for X-ray absorption spectroscopy using IFEFFIT. *J. Synchrotron Radiat.* **2005**, *12*, 537–541.
- (37) Bérodias, G.; Chevreton, M. Structural investigation of new ternary selenides MM', Se<sub>4</sub>. Compt. Rend. 1965, 261, 2202–2204.
- (38) Zhang, H.; Long, G.; Li, D.; Sabirianov, R.; Zeng, H. Fe<sub>3</sub>Se<sub>4</sub> nanostructures with giant coercivity synthesized by solution chemistry. *Chem. Mater.* **2011**, *23*, 3769–3774.
- (39) Li, D.; et al. Controllable phase transition for layered  $\beta$ -FeSe superconductor synthesized by solution chemistry. *Chem. Mater.* **2017**, 29, 842–848.
- (40) Lyubutin, I. S.; Lin, C.-R.; Funtov, K. O.; Dmitrieva, T. V.; Starchikov, S. S.; Siao, Y.-J.; Chen, M.-L. Structural, magnetic, and electronic properties of iron selenide Fe<sub>6-7</sub>Se<sub>8</sub> nanoparticles obtained by thermal decomposition in high-temperature organic solvents. *J. Chem. Phys.* **2014**, *141*, No. 044704.
- (41) Greenfield, J. T.; Kamali, S.; Lee, K.; Kovnir, K. A solution for solution-produced  $\beta$ -FeSe: elucidating and overcoming factors that prevent superconductivity. *Chem. Mater.* **2015**, *27*, 588–596.
- (42) Rousseau, D. L.; Bauman, R. P.; Porto, S. P. S. Normal mode determination in crystals. *J. Raman Spectrosc.* **1981**, *10*, 253–290.
- (43) Shatruk, M.; Chouai, A.; Dunbar, K. R. Influence of anions on the dimensionality of extended networks based on Cu<sup>I</sup> cations and 1,4,5,8,9,12-hexaazatriphenylene (HAT) ligands. *Dalton Trans.* **2006**, 124, 2184–2191.
- (44) Rudolph, J.; Jacob, C. R. Revisiting the dependence of Cu Kedge X-ray absorption spectra on oxidation state and coordination environment. *Inorg. Chem.* **2018**, *57*, 10591–10607.
- (45) Khammang, A.; Wright, J. T.; Meulenberg, R. W. Mechanistic insight into copper cation exchange in cadmium selenide semi-conductor nanocrystals using X-ray absorption spectroscopy. *Nat. Commun.* **2021**, *12*, No. 438.
- (46) Kau, L. S.; Spira-Solomon, D. J.; Penner-Hahn, J. E.; Hodgson, K. O.; Solomon, E. I. X-ray absorption edge determination of the oxidation state and coordination number of copper. Application to the type 3 site in Rhus vernicifera laccase and its reaction with oxygen. *J. Am. Chem. Soc.* 1987, 109, 6433–6442.
- (47) Zhou, Y.; Che, F.; Liu, M.; Zou, C.; Liang, Z.; De Luna, P.; Yuan, H.; Li, J.; Wang, Z.; Xie, H.; et al. Dopant-induced electron localization drives CO<sub>2</sub> reduction to C<sub>2</sub> hydrocarbons. *Nat. Chem.* **2018**, *10*, 974–980.
- (48) Zhang, J.; Liu, Y.; Liu, H.; Song, Y.; Sun, S.; Li, Q.; Xing, X.; Chen, J. Urchin-like Fe<sub>3</sub>Se<sub>4</sub> hierarchitectures: a novel pseudocapacitive sodium-ion storage anode with prominent rate and cycling properties. *Small* **2020**, *16*, No. 2000504.
- (49) Larumbe, S.; Gomez-Polo, C.; Pérez-Landazábal, J. I.; García-Prieto, A.; Alonso, J.; Fdez-Gubieda, M. L.; Cordero, D.; Gómez, J. Ni doped Fe<sub>3</sub>O<sub>4</sub> magnetic nanoparticles. *J. Nanosci. Nanotechnol.* **2012**, 12, 2652–2660.
- (50) Lamazares, J.; Gonzalez-Jimenez, F.; Jaimes, E.; D'Onofrio, L.; Iraldi, R.; Sanchez-Porras, G.; Quintero, M.; Gonzalez, J.; Woolley, J. C.; Lamarche, G. Magnetic, transport, X-ray diffraction and

Mössbauer measurements on CuFeSe $_2$ . J. Magn. Magn. Mater. 1992, 104–107, 997–998.